Acta Mechanica Sinica (2021) 37(6):954–969
https://doi.org/10.1007/s10409-021-01094-y

RESEARCH PAPER

Aerodynamic shape optimization of an urban maglev train

Z. X. Sun[1] · M. Y. Wang[1,2] · L. Y. Wei[1,2] · F. B. Kong[3] · G. W. Yang[1,2]

Received: 23 February 2021 / Revised: 25 March 2021 / Accepted: 1 April 2021 / Published online: 11 May 2021

Abstract
With rapid development of urban rail transit, maglev trains, benefiting from its comfortable, energy-saving and environmentally friendly merits, have gradually entered people's horizons. In this paper, aiming at improving the aerodynamic performance of an urban maglev train, the aerodynamic optimization design has been performed. An improved two-point infill criterion has been adopted to construct the cross-validated Kriging model. Meanwhile, the multi-objective genetic algorithm and complex three-dimensional geometric parametrization method have been used, to optimize the streamlined head of the train. Several optimal shapes have been obtained. Results reveal that the optimization strategy used in this paper is sufficiently accurate and time-efficient for the optimization of the urban maglev train, and can be applied in practical engineering. Compared to the prototype of the train, optimal shape benefits from higher lift of the leading car and smaller drag of the whole train. Sensitivity analysis reveals that the length and height of the streamlined head have a great influence on the aerodynamic performance of the train, and strong nonlinear relationships exist between these design variables and aerodynamic performance. The conclusions drawn in this study offer the chance to derive critical reference values for the optimization of the aerodynamic characteristics of urban maglev trains.

Keywords Urban maglev train · Aerodynamic characteristics · Cross validation · Kriging model · Genetic algorithm

1 Introduction

High-speed trains have always been popular in research for transportation all over the world. The wheel-rail train is a kind of vehicle pulled by adhesion force [1], whose operation speed is restricted by the speed limit of adhesive transmission between wheels and rails [2]. At the same time, the noise and vibration produced during operation will not only deteriorate the ecology, but also reduce comfort for passengers. Meanwhile, the non-ground-contact vehicle, which is, the maglev train, has attracted extensive attention of researchers. In 1971, the world's first maglev train, the Messerschmitt–Bölkow–Blolm (MBB) demonstration train, was exhibited in Munich, Germany [3]. The University of Tokyo, Japan, began to study high speed surface transport (HSST) medium and low-speed maglev technology in 1974 [4]. In 1984, UK opened the world's first commercial maglev railway, the Birmingham Line. In 1994, Southwest Jiaotong University of China built the first maglev railway test line, and conducted manned test in the meantime.

The aerodynamic effects of the train have a great influence on issues, like operation safety, energy saving, environmental protection, and ride comfort. The speed of maglev train is generally ranging from 90 km/h up to 600 km/h. The faster the train runs, the more devastating the aerodynamic problems are. Tyll et al. [5] carried out wind tunnel tests on maglev trains at speeds of about 240 km/h, and measured the values of aerodynamic lift force coefficient and drag force coefficient, which paved the way for the development and design of maglev trains. Huang et al. [6] studied the transient flow field generated by two maglev trains running at the speed of 430 km/h when passing by each other by means of the unsteady numerical simulation method. The results showed that the peak value of the instantaneous pressure on the surface was about twice as high as that of a single

Executive Editor: Xue-Ming Shao

✉ Z. X. Sun
sunzhenxu@imech.ac.cn

[1] Key Laboratory for Mechanics in Fluid Solid Coupling Systems, Institute of Mechanics, Chinese Academy of Sciences, Beijing 100190, China

[2] School of Engineering Science, University of Chinese Academy of Sciences, Beijing 101408, China

[3] CRRC Tangshan Co., Ltd Tangshan, Hebei 063000, China

open-line train. Gao et al. [7] simulated the meeting pressure wave of the maglev train, and evaluated the aerodynamic performance of the high-speed maglev test vehicle running at 500 km/h. They concluded that when the trains passed by each other, the largest pressure fluctuation appeared at the widest part of the vehicle.

The urban maglev train is a kind of small low-speed maglev train serving in the city. During operation, changes of drag, effect of crosswind and wind shear will affect the propulsion settings, lateral guidance and control system of the train, respectively. The aerodynamic behaviors of the urban maglev train are worth further exploring despite that the aerodynamic drag is not the most important factor acting upon the train. Wells and Colin [8] carried out an aerodynamic experiment of the concept maglev vehicle with a 1:12 scaled ratio in the low speed wind tunnel of Old Dominion University and obtained all the aerodynamic features and torques at different yaw angles. They found that large increase of lateral force and overturning moment had a significant adverse effect on the distribution of maglev force along the train body. According to historical data, Colin et al. [9] intensively studied the aerodynamic characteristics of low-speed urban maglev trains, especially the influence of environmental wind on the load of suspended electromagnet, which proved once again that the effect of cross wind would pose a great risk to the development of the maglev.

To further improve the aerodynamic performance of high-speed trains or maglev trains, the head shape optimization design tends to be one of the effective ways. The maglev train and the wheel-rail train can be regarded as long and thin bodies moving at high speed on the ground. The only difference of the two lies in their driving systems. Therefore, the streamlined aerodynamic shape design of maglev train is also supposed to play a key role in optimizing aerodynamic performance. Shu et al. [10] taking Shanghai high speed maglev train TR08 as the prototype, designed four new heads and studied their aerodynamic characteristics respectively. In the end they found that merely increasing the length of the streamlined head would lead to dramatic reduction of the aerodynamic drag and lift while other conditions stayed the same. Yao and Xu [11] also modified the shape of TR08 head, and designed four new head shape schemes. The simulation results revealed that if the compartment distance remained unchanged, that the length of the streamlined head is controlled within 6 to 7 m was able to well optimize the train aerodynamic characteristics. Zhou et al. [12] created three new head types in reference to TR08 head type and simulated the aerodynamic coefficients of different head maglev trains at different running speeds. After comparative analysis, they considered that the flat shuttle head type had the best aerodynamic optimization performance.

Basically, above optimization studies could be seen as the optimal selection method, which compares the aerodynamic performance of different head types of trains and selects the best design among them. However, this method requires engineers to be extraordinarily experienced while it still cannot guarantee that the selected scheme owns the optimal performance. Alternatively, aerodynamic shape design method based on optimization algorithms has gradually become a hot focus, whose biggest advantage is that it can improve the design efficiency and reduce the input cost. Currently, most of the aerodynamic shape optimization studies focus on high-speed trains. Based on a two-dimensional shape optimization, Kwon et al. [13], Lee [14] and Kim and Ok [15] performed a study about the influence of streamlined nose on the micro-pressure wave. Vytla et al. [16] carried out multi-objective optimization on geometric shapes of a high-speed train by setting up self-adaptive surrogate models. Krajnovic [17] optimized the shape of the train to improve its cross-wind stability and carried out the optimization of vortex generators for the purpose of drag reduction. Ku et al. [18] proposed a modeling function (VMF) parametric method for streamlined shape of high-speed trains, and then performed aerodynamic optimization on the base of VMF method. Based on the free-form deformation (FFD) method. Li et al. [19] carried out a multi-objective optimization of the aerodynamic performance of the CRH2 high-speed train in the open air. The relationships between the design variables and aerodynamic performance were intensively investigated. Zhang et al. [20] proposed a chaotic ant colony optimization algorithm with fine searching ability aimed to realize the multi-objective optimization design of high-speed trains. Through optimization, the aerodynamic drag and tail lift of the simplified train were obviously reduced, which proved the effectiveness of the method. Paniagua and García [21] applied genetic algorithm (GA) to the optimization design of the train head shape under two different operating scenarios. After analyzing the variance of the results, they summarized the influence of each design variable on the side force. Aiming at reducing the drag of the aerodynamic train model, Paniagua and García [22] adopted the surrogate model and genetic algorithms to achieve a reduction of 32.5% comparing to original reference geometry. Yao et al. [23] delineated the nonlinear relationship between the aerodynamic drag of high-speed train and the design variables of the nose by combining the multi-objective particle swarm optimization algorithm and support vector machine regression model. Zhang et al. [24] performed a multi-objective aerodynamic shape optimization to improve the aerodynamic performance of the high-speed train running on the embankment. The relationships between the design variables and the objectives were discussed, and the contributions of the primary factors to the optimization objectives were obtained. Yu et al. [25] performed a multi-disciplinary optimization, which taking the aerodynamic drag and load reduction factor as the design objectives. The final results showed that the aerodynamic

drag of optimized train was reduced by up to 4.15%, and the load reduction factor was reduced by up to 1.72%.

Due to the limited study on aerodynamic optimization of maglev rains, in the present study, aerodynamic optimization design based on optimization algorithms has been adopted as a brand new try, aiming to obtain the best aerodynamic performance of an urban maglev train within its design space. To mark the novelty with previous studies in surrogate based shape optimization, current study provides a new approach to construct the Kriging model, which makes use of the two-point infill criteria by maximizing the expectation. Meanwhile, in order to shorten the training period, instead of using the same training set for all the objectives, each optimization objective is corresponding to a specific training set. As discussed before, from the view of engineering application, aerodynamic optimization of an urban maglev train has been seldomly studied before, current study fills the void and gives out the basic relationship between the key design variables and optimization objectives, which could provide insight on the design of urban maglev trains. This study is comprised of seven sections. In the second section, the feasibility of the method adopted in this study is validated by comparing the results of wind tunnel test and numerical simulation. Related theories of Kriging model based on cross validation are introduced in detail in this section as well. In the third section, the computational model, domain and conditions of the numerical simulation are briefly presented. In the fourth and fifth sections, the realization of the parametric method of the train geometry and the complete flow chart of head optimization design are described respectively. In the sixth section, the optimization results are discussed by combining the optimal solution set and the results of aerodynamics coefficient. Finally, conclusions are summed up in the seventh section.

2 Numerical and optimization algorithms

The urban maglev train, including a leading car and a trailing car, is under investigation. The lift of the leading car and drag of the whole train are of primary concern, which are taken as objectives during aerodynamic optimization. These two objectives are chosen elaborately after discussing carefully with the engineering department. We try to maximize the former and minimize the latter in the present work. It should be noted that there actually should be a limit for the maximum of the lift of the leading car. However, confined by the design space of the design variables, maximizing the lift could be favorable for the balancing of the own weight of the leading car, and the value of the obtained optimal lift will never reach the maximum mentioned above. Since computational cost takes the major part during optimization, it will be unbearable to perform aerodynamic optimization directly by means of a global optimization method. In order to shorten the optimization period while not affect the optimization accuracy, the steady Reynolds averaged Navier–Stokes (RANS) method has been adopted for computational fluid dynamics (CFD) calculation, and the Kriging surrogate model on the base of cross validation method has been utilized to replace the CFD calculation for every sample generated in the optimization. In order to construct the final Kriging model, a two-point infill criterion has been implemented in present work. These methods and corresponding validations will be introduced in detail in this section.

2.1 CFD algorithms and validation

2.1.1 CFD algorithms

In this paper, commercial software STAR-CCM+ is used to study the aerodynamics of the urban maglev train. This software has the advantages of high computational efficiency and easy convergence of results, so it has been widely used in industrial applications. The governing equation used in the study is three-dimensional incompressible stationary N–S equations, which needs to be discretized by the finite volume method based on Roe format. The turbulence model adopted in the present paper is the shear stress transport (SST) k–ω model, which can improve the separation prediction in the near-wall region and has been used in various engineering applications [26]. Specifically, Li et al. [27] compared different RANS turbulence models for the evaluation of aerodynamic performance of trains in crosswind and found that the most accurate model for predicting the surface pressure of the train is SST k–ω, followed by realizable k–ε. The transport equations for SST k–ω model in detail are given in Ref. [28]. In addition, in order to control the number of grids in the boundary layer and ensure calculation accuracy, a standard wall function is used on the train wall [29].

2.1.2 CFD validation

This experiment is carried out in AVIC Aerodynamics Research Institute in Harbin, Heilongjiang. The maglev train model in the wind tunnel is shown in Fig. 1a, which is a 1:8 scaled model with windshields included. For CFD validation, the computational setup of domain and inlet conditions are kept exactly the same with experimental setup. Figure 1b shows the mesh distribution along the longitudinal section and in the boundary layer. It can be seen that the hybrid Cartesian grids are used in present work. Meanwhile, the wall functions are adopted to reduce the computational cost. $y+$ is kept in a range from 30 to 100 to ensure the effectiveness of wall functions. The mesh is locally densified to capture the flow details in specific places such as the gap between the

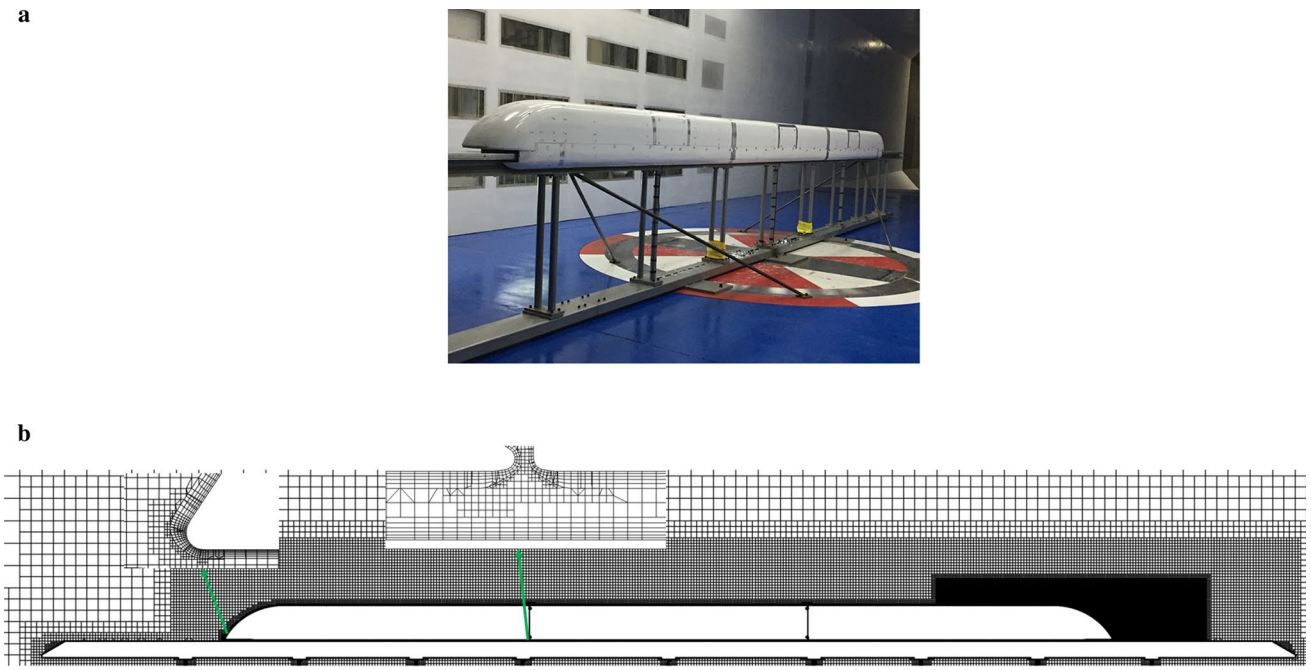

Fig. 1 **a** Wind tunnel test model and **b** distribution of spatial grid

train and the guideway, the windshield region and the wake region. The total amount of grids is about 31.33 million.

To simplify analysis, define drag force coefficient C_d and lift force coefficient C_l as follows:

$$C_d = \frac{F_d}{0.5\rho V_{ref}^2 A_{ref}}, \tag{1}$$

$$C_l = \frac{F_l}{0.5\rho V_{ref}^2 A_{ref}}, \tag{2}$$

where A_{ref} is the projected area of the train in the x direction, F_d is the drag force, F_l is lift force, V_{ref} is the incoming flow velocity, and ρ is the density of the incoming flow.

Table 1 shows the comparison of aerodynamic drag and lift coefficients from experiments and numerical simulations. It is clear that the errors of aerodynamic loads of each car are within 3.5%, indicating that both the numerical algorithms and the mesh configuration can predict precisely the flow field around the train and can be further used for the CFD calculation during aerodynamic optimization.

2.2 Cross-validation based Kriging surrogate model

2.2.1 Kriging surrogate model

The Kriging model includes the regression model and the related model [30]. Although the functions of the two models are different, they are closely related to the prediction ability of Kriging model. By using the likelihood estimation of the maximum response value, the problem of solving the parameters of the related model is transformed into a nonlinear and unconstrained maximization problem, which is the construction process of the Kriging model in general. This study gave up the traditional modeling method to directly minimize the prediction error of training sample points on the basis of cross-validation method. Then the Kriging model is further constructed after the optimal solution is acquired.

Table 1 Comparison of CFD and experimental results

	Total-C_d	Head-C_d	Head-C_l	Middle-C_d	Middle-C_l	Tail-C_d	Tail-C_l
Exp	0.3368	0.0846	0.4169	0.0864	− 0.0247	0.1658	0.2776
CFD	0.3279	0.0831	0.4058	0.0843	− 0.024	0.1605	0.2831
Error (%)	− 2.64	− 1.77	− 2.66	− 2.43	− 2.83	− 3.20	1.98

2.2.2 Cross validation method

Cross validation is a commonly used statistical analysis method for modeling, which can evaluate the generalization error of the machine learning model [31]. Even if the information of the sample set is scarce, this method can still realize the construction of the surrogate model without a separate test set and guarantee high prediction accuracy. The common cross validation methods include leave-one-out cross validation [32], leave-p-out cross validation [33], *k*-fold cross validation [34] and 3×2 block cross validation [35]. At present, the theoretical system of cross validation is not yet fully mature, and this method is vulnerable to the influence of data set segmentation, so one should carefully choose the data set segmentation according to different problems. It has been proven that it is feasible to segment the data sets of regression problems by random methods, which ensures the correctness of the method used in this paper to a certain extent.

The basic idea of cross validation method is, according to certain standards, the original data is divided into N groups. Among them one group is selected as the validation set and the other groups constitute the training set to establish the surrogate model. Then the prediction error of the validation set is calculated and recorded by the model. This process is repeated until each set of datasets is available and only once as the validation set. Finally, the averaged value of all the prediction errors is treated as the performance index of the surrogate model, referring to which the parameters of the relevant model can be easily determined. In this paper, when the cross validation method is applied to determine the optimal parameters of the surrogate model, the model parameters corresponding to the minimum average of the prediction error of all validation sets are taken as the final model parameters.

2.2.3 Two-point infill criterion

The point addition criterion is a standard to select new sample points in the process of modeling in order to improve the accuracy of the surrogate model. During sub-optimization, the adding point criterion can optimize the selection of objectives and exert a direct impact on the optimization performance. There are many kinds of adding point criteria, among which the most popular ones are minimizing the response surface criterion and maximizing the expectation criterion. Although the former is compatible with any surrogate model, it is more suitable for solving simple optimization problems or problems with enough training sample points, otherwise a local optimal solution is more likely to be obtained. The latter makes full use of the property that the Kriging model can predict the variance of unknown points, and can not only derive the optimal solution of the surrogate model, but also take into account the influence of the uncertainty of the prediction point, turning out to be a more efficient method.

It is necessary to find the region covering the prediction points with large uncertainty after adding points near the optimal solution. However, the multi-peaks of the expected function will make it more difficult to find the optimal solution. In order to solve this problem, Gao and Wang [36] proposed a multi-point addition criterion, which required that the contemporary optimal solution and the prediction standard deviation should be added to each iteration. In this paper, the addition criterion is modified appropriately: two points are added in each iteration, and the genetic algorithm with strong global optimization ability is used to determine the points with large prediction standard deviation.

2.3 Genetic algorithm

In 1975, on the basis of the idea of "survival of the fittest", Holland [37] proposed the genetic algorithm for the first time. The global searching process of genetic algorithm can be achieved as follows: the parent individual is selected from the random initial population, and the evolved offspring population is generated by selection, crossing and mutation. With the continuous evolution of the population, the fitness of the members is also gradually improved, and finally the optimal solution of the optimization problem can be decided according to the individuals with optimal fitness.

The NSGA-II adopted in this paper is one of the most widely used and effective multi-objective genetic algorithms. The algorithm, put forward by Deb et al. [38] in 2000, can directly solve the multi-objective optimal solution set (Pareto solution set), which makes up for the shortcomings of the traditional multi-objective optimization algorithm. The algorithm flow is as follows: firstly, the initial population with N individuals is sorted un-dominantly, and two populations are merged as one after the offspring population with N individuals is produced by selection, crossing and mutation. Then, the new population with the size of $2N$ is classified layer by layer, and individuals are sorted according to the non-inferior relationship. After that, from excellent to inferior, each individual is labeled with a fitness value, and the first N individuals are selected as the new parent population. The above process is repeated until the termination condition is reached.

2.4 Validation of multi-objective optimization strategy

Aimed at testing the prediction accuracy of the CV-based Kriging model and the efficiency of two-point infill criterion, the Branin function is chosen as the test function, as shown below:

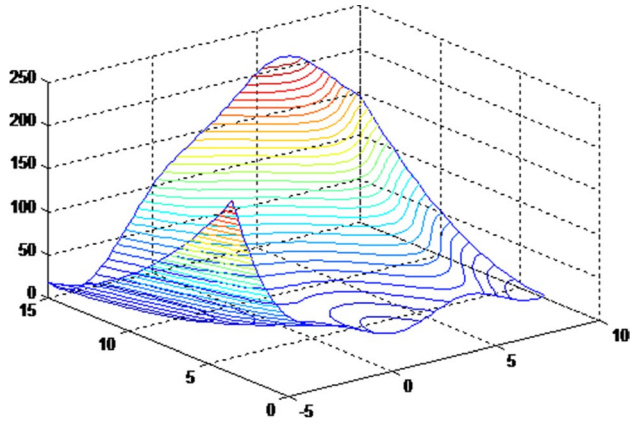

Fig. 2 Branin function surface

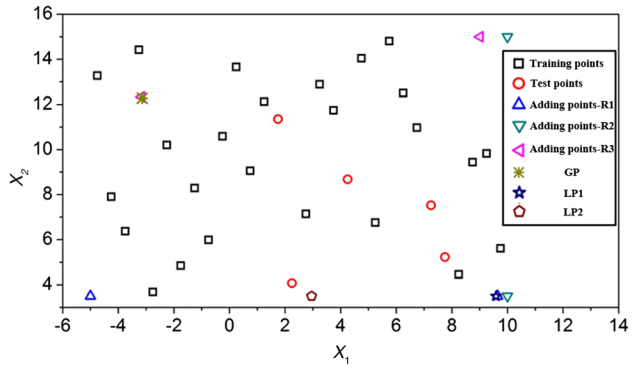

Fig. 3 Distribution of sample points

$$f(x) = \left(x_2 - \frac{5.1}{4\pi^2}x_1^2 + \frac{5}{\pi}x_1 - 6\right)^2 + 10\left(1 - \frac{1}{8\pi}\right)\cos x_1 + 10, \tag{3}$$

$$-5 \le x_1 \le 10,\ 3.5 \le x_2 \le 15. \tag{4}$$

In the given design space, a global minimum exists at point (− 3.142, 12.275) with a value of 0.3979, while two local minimums emerge at point (9.588, 3.5) and point (2.955, 3.5) with values of 1.3067 and 1.7202 respectively. Figure 2 illustrates three-dimensional surface of the Branin function. The Branin function varies from a minimal value smaller than 1 to a maximal value bigger than 200, which can efficiently test the prediction capability of the Kriging model.

In order to extract the initial training samples evenly distributed in the design space, the maximin Latin Hypercube Sampling method has been adopted. 30 initial samples have been selected, 25 of which are set to be training samples while the rest 5 points to be testing points.

After adding points for three times, the Kriging model with the prediction error within 1% has been constructed. Figure 3 shows the distribution of initial sampling points and the added points of three times. It is apparent that few sampling points are be observed around the global optimum point (GP) and local optimum points (LP1 and LP2). Since GP, LP1 and LP2 are very close, the Kriging model constructed by the initial sampling points cannot tell them apart. The optimal value obtained by this Kriging model is located near LP1. As a result, the added points in the first round are about the position of LP1 and the boundary. After adding points for the first time, the prediction accuracy near the position of LP1 has been increased, but no apparent improvement is found near LP2. The optimal value predicted by the rebuilt Kriging model lies near the position of LP2. After adding points for the second time, the prediction accuracy near LP1 and LP2 has been improved and the new optimal value gets close to GP. However, the accuracy for the optimum can't meet the requirement at this stage and adding points for the third time is demanded. Finally, the prediction accuracy near all three places has been greatly improved. After adding points for three times, the constructed Kriging model can perfectly predict the Branin function.

Figure 4 exhibits the prediction errors of the Kriging models at three different stages. Due to the scarce distribution of sampling points near the boundary, it is no surprise that the maximal prediction errors usually appear at the boundary. Similar to Fig. 3, the maximal error region is also the maximal variance region. The prediction error of the Kriging model can be greatly decreased by adding the point with maximal variance. As shown in Fig. 4, the prediction error becomes smaller and smaller as the adding point times increase. After adding points for the third time, the prediction error within the design space gets close to zero. The predicted global optimum is 0.4007 with a location at (3.16, 12.32). The averaged prediction error for the five sampling points is 0.23%. Consequently, the combination of the CV-based Kriging model and two-point infill criterion can add points more reasonably and improve the prediction accuracy and efficiency prominently.

Different Kriging models apply to different objectives for multi-objective problems. If one single Kriging model is used for different objectives, the prediction accuracy can be damaged. In present work, separate Kriging models have been constructed for different objectives to elevate the prediction accuracy. The same initial sampling set is used for both Kriging models to reduce the number of training samples. However, the added points are different during the reconstruction of each Kriging model.

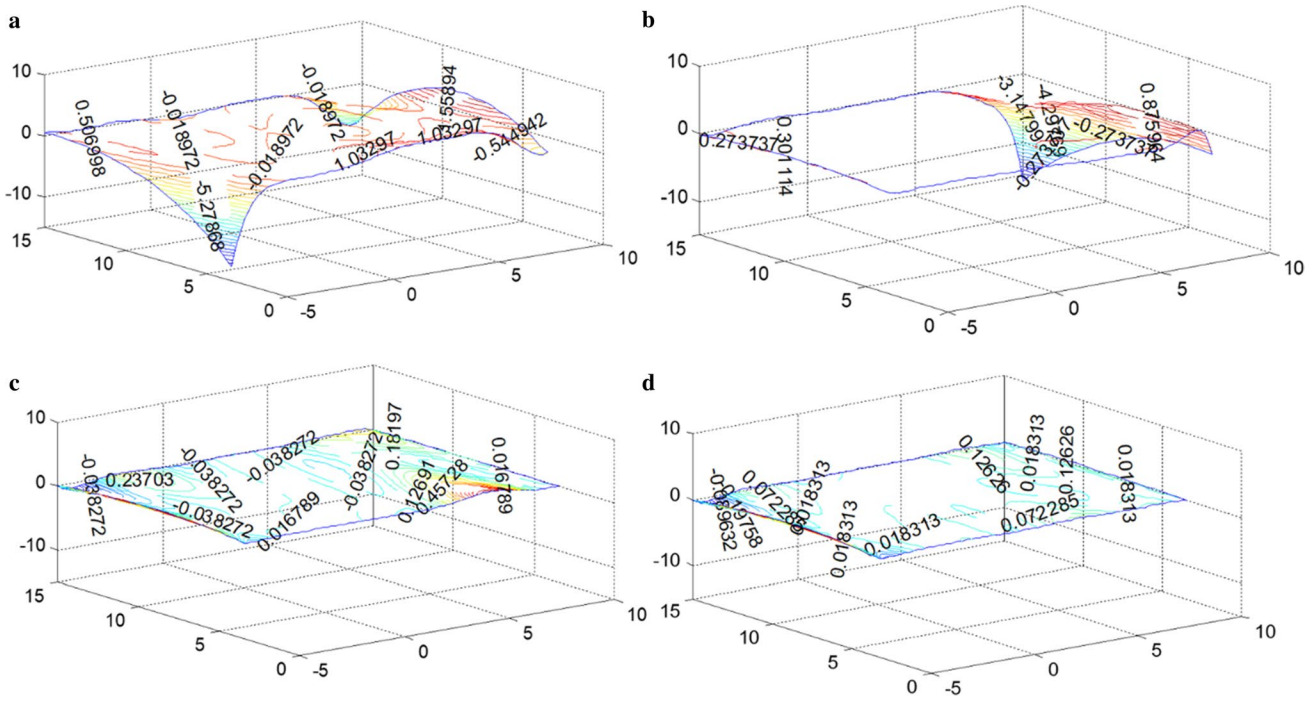

Fig. 4 Error distribution in different iterations: **a** before adding points; **b** adding point for the first time; **c** adding point for the second time; **d** adding point for the third time

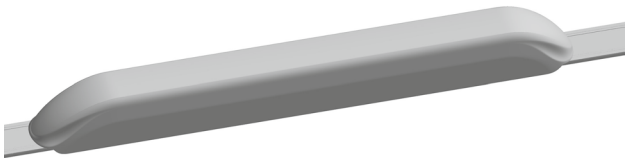

Fig. 5 Urban maglev train model

3 Computational model, domain and conditions

The computational model of the maglev train is shown in Fig. 5. As shown below, the guide way for the train is considered as well for its essential role to the aerodynamic performance. The maglev train is running over the guideway with a clearance of 10 mm, and the running speed is 200 km/h.

The hybrid Cartesian/prism grids are adopted and 10 layers of prism grids are generated with an increasing ratio of 1.1 and a total length of 30 mm, which is in accord with the mesh configuration in Sect. 2.1.2. With use of the wall functions near the train surface, the value of $y+$ among 30–100 could guarantee the computational requirement of SST turbulence model. The grids on the longitudinal section of the domain are shown in Fig. 6. Moreover, additional densified zone is utilized between the bottom of the train and the guideway, so as to keep the mesh fine enough to capture the flow details there. The grids in the gap between the guideway and the maglev train are crucial to the aerodynamic performance, which are also shown in Fig. 6.

The computational domain is shown in Fig. 7. Marking the height of the train H as the characteristic length, referring to whom the distance from the inlet boundary to the leading nose is about $14H$, while the distance from the trailing nose to the outlet boundary is $38H$. The width and height of the domain are $30H$ and $22H$, respectively.

The running speed of the incoming flow is 200 km/h, which can be regarded as incompressible. In this paper, the incompressible solver is adopted for the simulation of the urban maglev train, the velocity inlet and pressure outlet boundaries are utilized. For the lateral and upper boundaries in the far field, we just make use of the slip wall boundary. Comparing the train model, the side wall and upper wall are far enough to affect the flow field near the train model. The use of slip wall condition or symmetry condition will not affect the prediction of aerodynamic force coefficients. As a result, the slip wall boundary conditions are adopted here. And for the ground and the guideway, considering their relative movement to the train, a moving wall condition with the speed of the incoming flow is prescribed on these two boundaries.

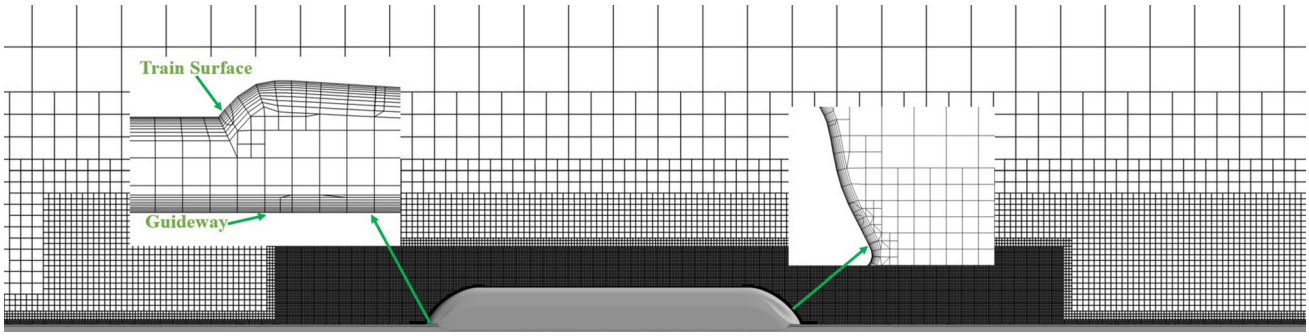

Fig. 6 Grids on the longitudinal section of the domain

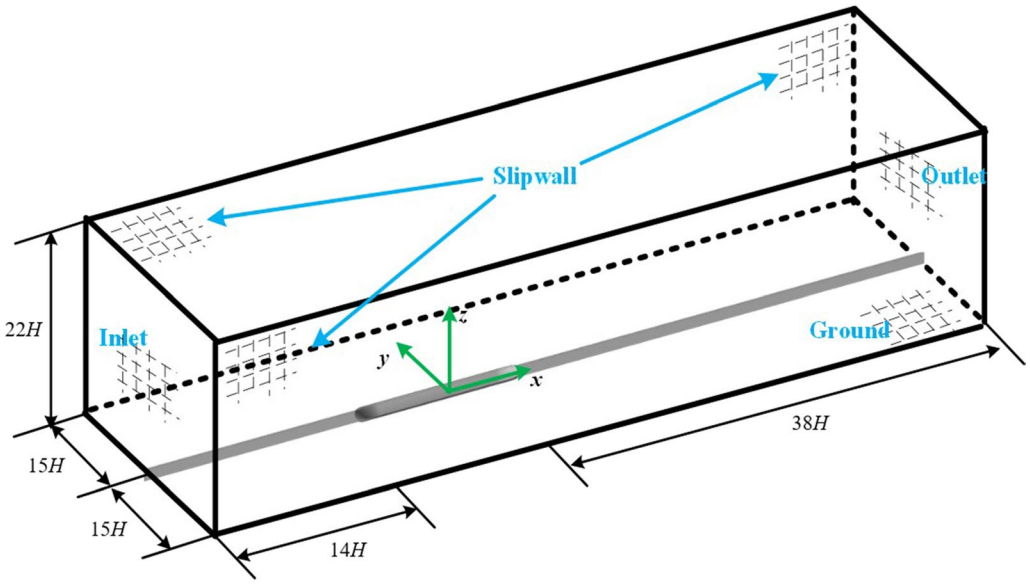

Fig. 7 Computational domain

4 Parametric approach

Parameterization methods play a crucial role in aerodynamic shape optimization. An excellent parametric method can not only reflect the deformation of the shape, but also shorten the optimization period to a certain degree. The local shape function (LSF) method is utilized in present work for the parametrization of the urban maglev train, which controls the deformation by only a few design variables and keeps the smooth transition between adjacent surfaces as well. This method can be achieved with easy access. For LSF parametrical method, regions that need to be deformed should be divided separately at first. Grid discretization should be performed then on each region so that the coordinates of each grid are plotted. Shape functions should be introduced at this stage, which should guarantee the smooth transitions at surface boundaries. A weight coefficient W_i then is designated to each shape function, which can determine the maximum deformation in each region. Judging from the specific shape functions and corresponding weights, the increments of all the grids can be calculated. The final deformed shape can be compiled by combining the increments for each grid.

It is key to choose reasonable shape functions since different shape functions can lead to different deformations. Inappropriate shape functions can result in undesired surfaces and contaminate the optimization results. The commonly used shape functions include trigonometric functions, exponential functions and logarithmic functions while some other complicated functions such as polynomial functions and spline functions are also employed. In present work, the trigonometric functions are chosen as the shape functions.

Due to the symmetrical structure, parameterization can be performed only on half of the train surface. Once performing deformation on the train surface, the final deformed surface can be mirrored on the symmetrical

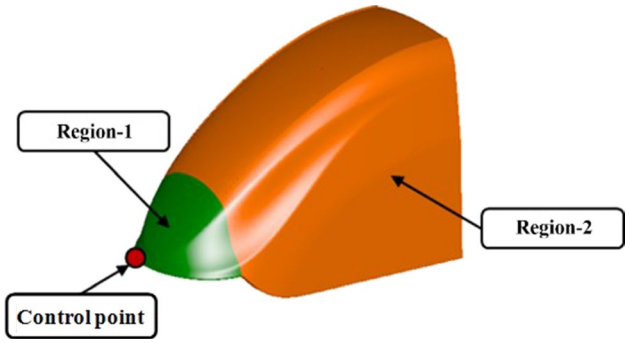

Fig. 8 Deformation regions and the control point

Table 2 Design variables and design space

Design variables	Controlling region	Range (mm)
W_1	Length of the streamline	(− 550, 550)
W_2	Nose height	(− 20, 40)

plane. As stated previously, current study has a close tie with the engineering design of modern urban maglev trains. After discussing with the engineering department, some design variables such as the cross section of the streamlined shape, the skirt plate along the guideway should be kept invariant. What can be changed are only the nose height and length of the streamline but in a limited range. To achieve the deformation considering these two variables, two control regions are divided, as shown in Fig. 8. It should be noted that when shape deformation is performed, both the leading streamline and the trailing streamline are deformed simultaneously. The nose height is controlled by Region-1, while the streamlined length is controlled by Region-1 and Region-2. One control point is attached on the nose tip, the y coordinate of which is chosen as the design variable W_1 while the x coordinate W_2.

Table 2 shows the control regions related to different design variables and ranges for different design variables. The design space is chosen very reasonably, with the practical constraints taken into consideration. The maximum cross-section and maximum width in the bottom are kept unchanged during optimization. No matter how design variables vary in this design space, the nose tip cannot intersect with the guideway and smooth connection between the streamline and the train body must be ensured.

Figure 9a, b demonstrate the shape deformations when encountering different values of W_1 and W_2. It meets the demand that the surface keeps smooth in the deformation zone, and the different deformation regions keep fluent connection as well. As a result, the LSF parametric method can be used for aerodynamic optimization for the urban maglev train.

5 Optimization strategy

5.1 Whole optimization process

Although the concept of Kriging surrogate model is well informed in the present optimization, it is still very necessary to design the optimization process. The optimization result would have been easily contaminated should some steps in the process go wrong. If this ever happens, the optimal results will not be acquired. The optimization process in present paper is illustrated in Fig. 10, and the steps in detail are as follows.

(1) Perform shape parameterization on the basis of the original urban maglev train model, decide the design

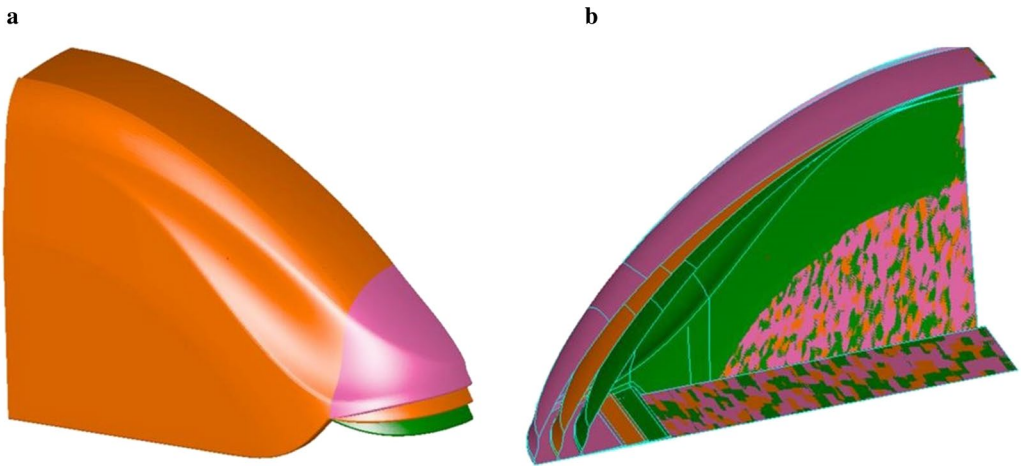

Fig. 9 Deformation demonstration: **a** nose height and **b** streamline length

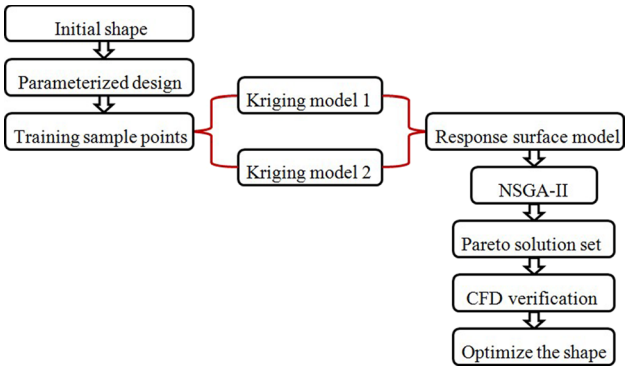

Fig. 10 Optimization process

space by corresponding geometric constraints, and extract a number of initial sampling points by the maxmin Latin hypercube sampling method.

(2) By means of real-coded NSGA-II and two-point infill criterion construct Kriging surrogate models for each objective according to the training set.

(3) Incorporate the two Kriging models into the final Kriging model set acting as the final surrogate model where NSGA-II works on.

(4) Calculate the Pareto set through the optimization on the Kriging model set by NSGA-II.

(5) Choose specific points in the Pareto set for CFD validation, so as to decide whether the Kriging models meet the accuracy requirement or not. If the requirement is met, the final optimal shape can be decided by proper decision and the optimization is finished. Otherwise, go back to step (2), and rebuild the Kriging models with more sampling points.

5.2 Construction of CV-based Kriging model

5.2.1 Process to construct the CV-based Kriging model

The way to construct a Kriging model merely comprises the process to decide the relevant coefficients. However, when introducing the two-point infill criterion, this process shifts to an optimization process. Figure 11 shows the construction process of CV-based Kriging model, which is illustrated as follows:

(1) Select the initial training samples, which is introduced in the previous section.

(2) Construct Kriging models by cross-validation criterion: firstly, the initial training samples are divided into N groups. One group of these training samples are chosen randomly as the testing set, while the other $N-1$ groups serve as the training set. Each one of $N-1$ groups builds up a sub-Kriging model. For the purpose of maintaining the advantages of both gradient algorithms and global optimization methods, we use the genetic algorithm and pattern search algorithm together during optimization. The initial values of the relevant coefficients for each sub-Kriging model are set to be the same. The initial values required by the pattern search algorithm are provided by the genetic algorithm. During optimization with the genetic algorithm, the pattern search algorithm determines the final values of relevant coefficients for each sub-Kriging model in each iteration. The built sub-Kriging model will be used to predict the values over the test set, and the averaged prediction error for the N groups is treated as the objective

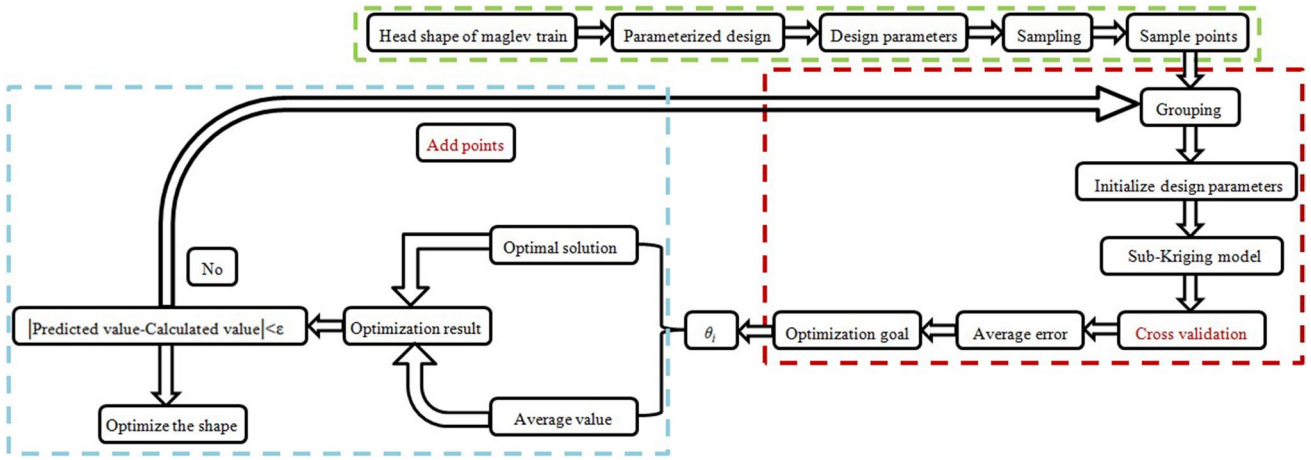

Fig. 11 Construction process of Kriging model based on two-point infill criterion

$$fit = \%RSME/N, \tag{5}$$

which can guide the direction to get the optimal values of relevant coefficients. The averaged prediction error is defined as below:

$$\%RMSE = \frac{100\sqrt{\frac{1}{n_s}\sum_{i=1}^{n_s}\left(y_i - y_i^{(p)}\right)^2}}{\frac{1}{n_s}\sum_{i=1}^{n_s} y_i}, \tag{6}$$

where n_s denotes the number of test samples, y_i denotes the accurate value and $y_i^{(p)}$ denotes the prediction value.

(3) Adding point process: After building the Kriging model, optimization is performed by NSGA-II to calculate the positions where the optimal value and the maximal variance are. The exact values of these two points can also be obtained by CFD calculation. Comparing the differences between prediction and CFD calculation, the Kriging model will be seen as the final model if the error meets the requirement. Otherwise, these two points should be added to the initial training set to rebuild the Kriging model, as instructed in step (2). When adding points, the division number N should be kept unchanged, and these two points should be added to each training group to ensure each sub-Kriging model can make full use of the information from these two points, so that each the prediction accuracy of sub-Kriging model can be guaranteed.

5.2.2 Construction of CV-based Kriging model with different optimization objectives

Two Kriging surrogate models are built for H-C_l and T-C_d respectively in present paper. Based on the given design variables and design space, 15 initial sampling points are finally chosen by means of Latin Hypercube method. These sampling points are divided randomly into five groups through 3-folded cross validation method. The two-point infill criterion has been implemented for the construction of each Kriging model. When both Kriging models meet the accuracy requirement, the final Kriging model set can be established by combining two Kriging models together, which gives insights for multiple objective optimization.

According to the different range of each target in the design space, the accuracy of each Kriging model needs to be clearly required to reduce the calculation time of the flow field. The variation of T-C_d in the design space is relatively small. A prediction accuracy error of 2% near the optimal area is decided for the Kriging model of T-C_d, and 3% for the other places. Meanwhile, H-C_l varies significantly in the design space, the maximum of which can be two times larger than the minimum. Consequently, a prediction accuracy error of 3% is chosen for the design space.

Table 3 Parameters of two sets of Kriging surrogate models

Kriging	Number of iterations	Predicted value	CFD	Error (%)	Average error (%)
KL	4	0.283	0.285	0.70	2.67
KD	4	0.171	0.168	1.79	1.86

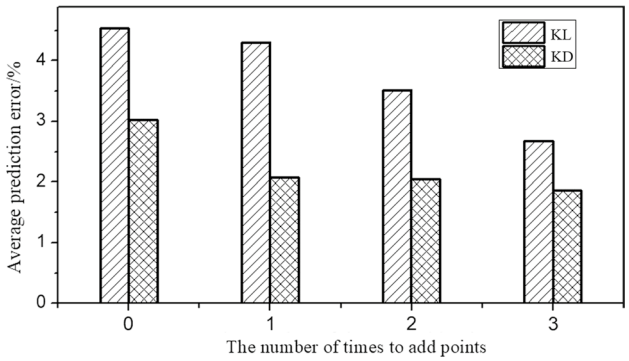

Fig. 12 Average prediction error of Kriging model in design space in the process of adding points

The Kriging models of H-C_l and T-C_d are named as KL and KD for convenience. Table 3 shows values of key parameters of two built-up Kriging models. It is obvious that both KL and KD meet the accuracy requirement after four iterations. The prediction error of KL near the optimal region is smaller than that of KD, while the averaged prediction error of KL is larger than that of KD.

Figure 12 shows the variation of the averaged prediction error of KL and KD along with the point adding times. As the number of sampling points increases, the prediction errors of KL and KD both decrease. However, the prediction error of KD falls behind that of KL all the time, in that H-C_l is more sensitive to the design variables compared to T-C_d and varies vastly in the design space.

6 Results and discussions

6.1 Analysis of the Pareto set

To verify the prediction accuracy of the Kriging model during each time the points are added, the Pareto set is delineated when optimizing on the Kriging model by means of NSGA-II. Six points are chosen from the Pareto set as the testing points. If the prediction accuracy of any of these six points lag behind the requirement, the Kriging surrogate

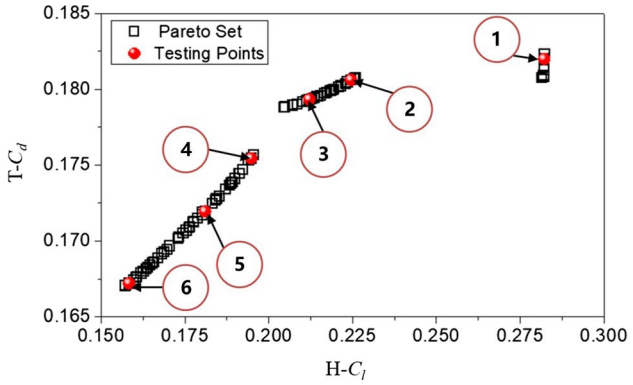

Fig. 13 Pareto solution set obtained by adding points for the second time and the location of the test sample point

Table 4 Prediction accuracy of test sample points (adding point for the third time)

Sample point number	Aerodynamic coefficient	Predicted value	CFD	Error (%)
1	H-C_l	0.2822	0.2847	−0.878
	T-C_d	0.1820	0.1809	0.608
2	H-C_l	0.2245	0.2232	0.582
	T-C_d	0.1806	0.1813	−0.386
3	H-C_l	0.2121	0.2095	1.241
	T-C_d	0.1794	0.1781	0.730
4	H-C_l	0.1947	0.1928	0.985
	T-C_d	0.1755	0.1734	1.211
5	H-C_l	0.1810	0.1795	0.836
	T-C_d	0.1720	0.1711	0.526
6	H-C_l	0.1583	0.1597	−0.877
	T-C_d	0.1672	0.1686	−0.830

model will be considered inaccurate and should be rebuilt during next iteration.

To throw light upon the following analysis, the drag of the whole train and the lift of the leading car are denoted as T-C_d and H-C_l. Figure 13 shows the Pareto set drawn after adding points for the third time, in which three distinct parts are observed. The two bottom parts distribute almost linearly and are located relatively close to each other, while the upper part is far away from the bottom two. Six points are chosen randomly from the Pareto set for accuracy validation, one of which is from the upper part while the others are from the other two parts.

Table 4 lists the prediction values and the CFD calculation values of H-C_l and T-C_d for the six testing points in Fig. 13. It could be found that the maximum prediction error for H-C_l is 1.241% while that of T-C_d is 1.211%, which both meet the accuracy requirement. The averaged prediction error of H-C_l is about 0.9% around the optimal zone, while the averaged prediction error of T-C_d is 0.715% around the optimal zone. As a result, after adding points for the third time, the Kriging models can be seen as the final model with sufficient accuracy and the obtained Pareto set is the final optimal set. Since no single optimal point exists for multi-objective optimization, the first testing point is chosen as the final optimal solution for analysis, and its aerodynamic performance will be discussed in detail in the following sections.

Table 5 Values of the design variables for the optimal shape

Shapes	W_1 (mm)	W_2 (mm)
Prototype	0	0
Optimal shape	413	35

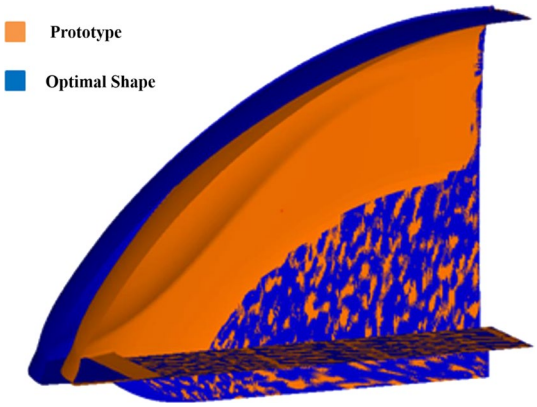

Fig. 14 Geometric shapes of the prototype and optimal models

6.2 Shape comparison before and after optimization

Since what has been discussed in the present paper comes from the practical engineering problem, the design space for optimization is literally confined with limited regions. As a consequence, the optimal shape can not warp too much. Table 5 shows the values of the design variables for the optimal shape. It can be found that the length of the streamlined head increases by 413 mm while the height of the nose grows by 35 mm.

Figure 14 shows the geometric shapes of the prototype and optimal models. After optimization, the length of the streamlined head is stretched obviously and the nose tip is lifted slightly. Meanwhile, no change is observed at the bottom and the maximum longitudinal section, which proves the efficiency of the LSF parametric method.

6.3 Comparison of aerodynamic performance before and after optimization

6.3.1 Comparison of the flow field before and after optimization

Figure 15 exhibits the pressure contour on the surface of the train as well as on the longitudinal section of the domain for the prototype and optimal model. Obvious high pressure can be observed on the leading and trailing nose tip for models before and after optimization. Vortex shedding can be found in the near wake zone. After optimization, the streamlined head has been lengthened, which relieves the negative pressure on the transition zone. Thanks to the rise of the nose tip, the incoming flow can easily get into the clearance between the bottom of the train and the guideway, resulting in stronger positive pressure on the bottom of the train. These two factors join hands together to generate greater lift of the leading car. A longer streamlined nose can improve the aerodynamic performance of the whole train. On the other hand, disturbance effect of the flow separation on the surface of the trailing nose decreases, which helps to bring down the drag of the trailing car.

The iso-surfaces of Q criterion at 1000 for the prototype and optimal shape are shown in Fig. 16. It can be observed that complex vortex system exists in the near wake. Two evident asymmetric vortices dominate and smaller vortex structures are also found near the nose tip. Compared to the prototype, the small vortices near the nose tip for the optimal model grow weaker, as well as the two asymmetric structures. Due to the weakness of vortex structures in the wake region, the aerodynamic performance of the trailing car is largely promoted.

6.3.2 Comparison of aerodynamic loads before and after optimization

Aerodynamic lift of the leading car and drag of the whole train are the optimization objectives in the present paper. Since the streamlined shapes of the leading car and trailing car are exactly the same, changes of the streamlined shape not only affect the aerodynamic performance of the leading car, but also that of the trailing car. As a result, when performing aerodynamic shape optimization, the aerodynamic performance of the leading car and trailing car should be considered together.

The coefficients of aerodynamic loads of the leading car and trailing car before and after optimization are given in Table 6. Aerodynamic lift of the trailing car is always higher than that of the leading car regardless of the models. The drag coefficient of the trailing car can be twice as large as that of the leading car. After optimization, aerodynamic lift of the optimal model is increased by 33.25% while that of the trailing car is reduced by only 1.78%. Meanwhile, the drag of the leading car remains constant before and after optimization while that of the trailing car drops by 6.42%.

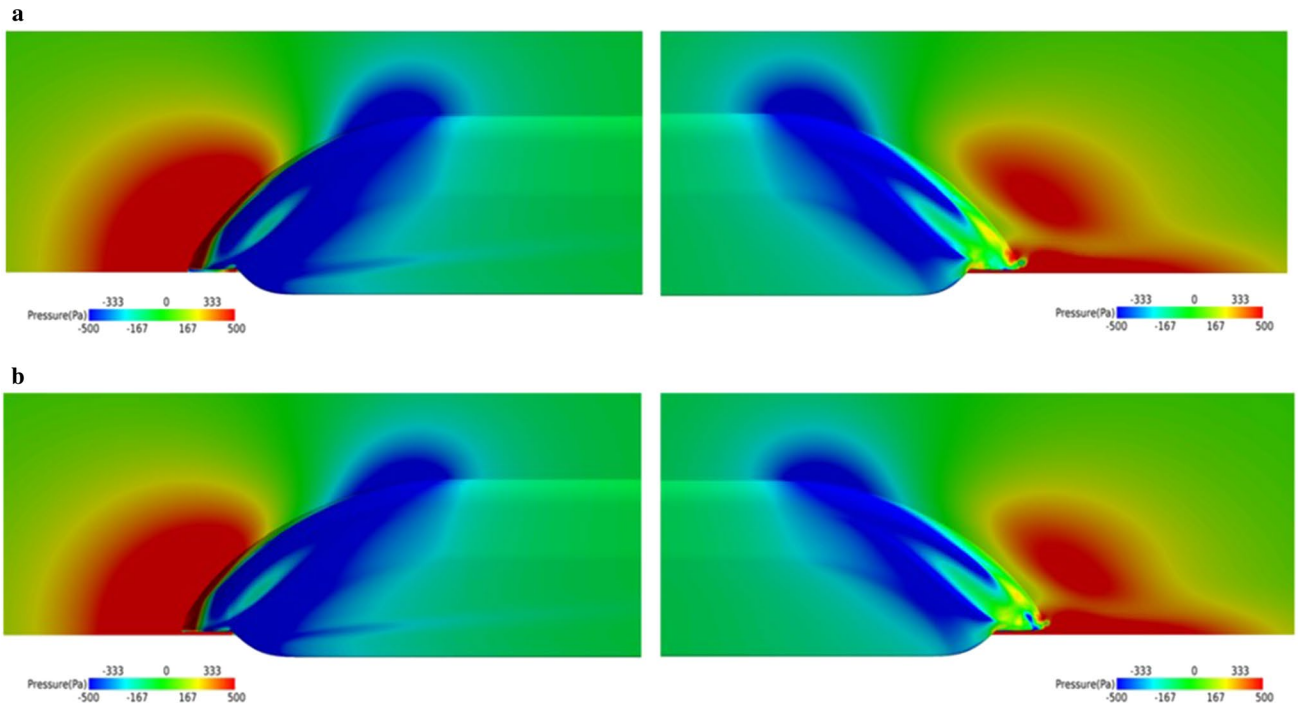

Fig. 15 Pressure contour on the streamlined shape and the longitudinal section: **a** original scheme and **b** optimization scheme

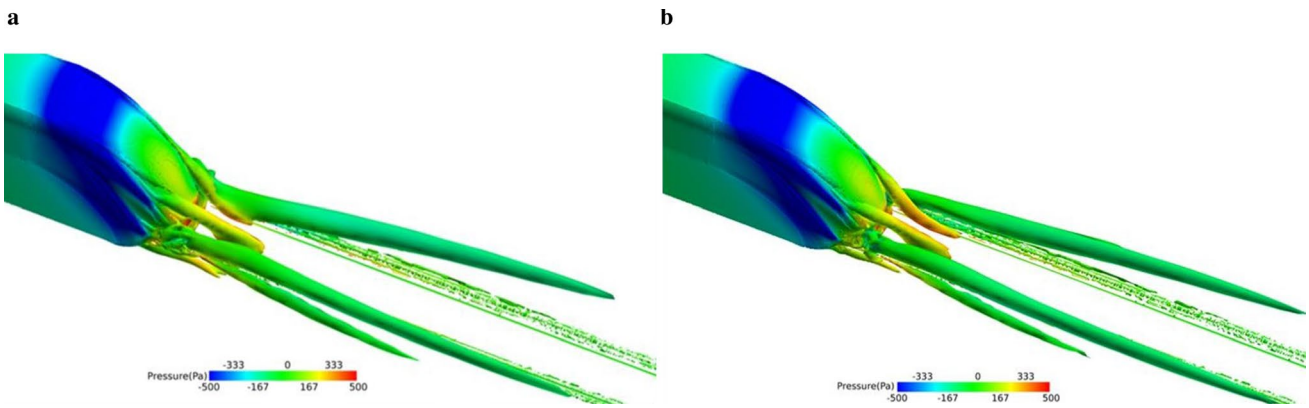

Fig. 16 Iso-surface of Q-criterion of tail car: **a** original scheme and **b** optimization scheme

Table 6 Aerodynamic drag coefficient (C_d) and lift coefficient (C_l) before and after optimization

	Leading-C_l	Trailing-C_l	Leading-C_d	Trailing-C_d	Total-C_d
Original scheme	0.213	0.732	0.059	0.131	0.189
Optimization scheme	0.283	0.719	0.059	0.122	0.181
Reduction rate (%)	− 33.246	1.784	0.000	6.418	4.441

Table 7 Comparison of viscous drag coefficient (C_d-Vis) and inviscid drag coefficient (C_d-Inv) of each carriage before and after optimization

	Head-C_d-Vis	Tail-C_d-Vis	Head-C_d-Inv	Tail-C_d-Inv
Original scheme	0.0477	0.0393	0.0108	0.0914
Optimization scheme	0.0476	0.0393	0.0109	0.0830
Reductionr rate (%)	0.21	0.000	− 1.0853	9.1692

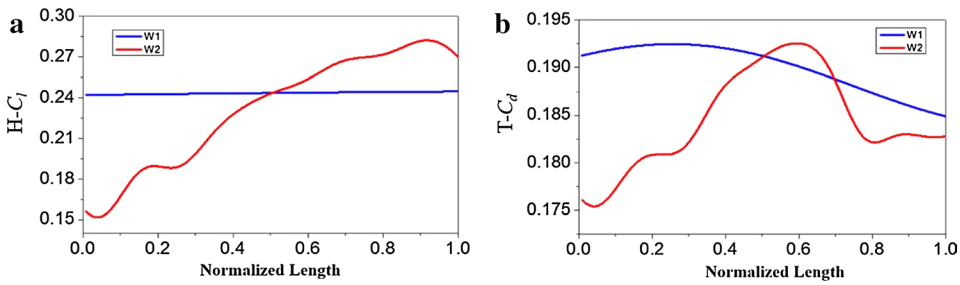

Fig. 17 Relationships of design parameters and optimization objectives: **a** H-C_l and **b** T-C_d

Taking the whole train into consideration, aerodynamic drag of the whole train is reduced by 4.44%.

In order to give a deeper understanding of why aerodynamic drag is reduced, Table 7 lists the inviscid drag coefficients and viscous drag coefficients of the leading car and the trailing car before and after optimization. The viscous drag coefficient of the leading car is slightly larger than that of the trailing car. However, the inviscid drag coefficient of the leading car is much smaller than that of the trailing car. The viscous drag stays almost constant during the optimization. Although the inviscid drag grows slightly for the leading car after optimization, that of the trailing car falls significantly, indicating that optimization of aerodynamic drag for the urban maglev trains should pay more attention to the trailing car.

6.4 Relationship between design variables and objectives

Insights from the relationship between design variables and objectives can be of great significance to practical engineering. With use of the final Kriging models, relationships between the aerodynamic loads and two design variables can be acquired. Ranges of design variables are both normalized to make easy comparisons. As shown in Fig. 17, the length of the streamlined shape has a subtle influence

on aerodynamic lift the leading car. Aerodynamic lift of the leading car climbs up slightly along with the increase of the length of the streamlined head. On the contrary, aerodynamic lift of the leading car gets affected severely by the length of the streamlined head. Non-linear relationship is observed in the current design space. Aerodynamic lift grows as the length increases when the length is less than 0.9 and then it reduces. Aerodynamic drag of the whole train behaves nonlinear effect from the two design variables. More complicated relationship exists between aerodynamic drag and the nose height. Generally speaking, more prominent influence of the nose height is found on aerodynamic loads, which should be more focused on during the optimal shape design of urban maglev trains.

7 Conclusions

Targeted at optimizing the aerodynamic shape of the urban maglev train, an optimization strategy has been proposed in the present paper. The cross-validation based Kriging surrogate model is adopted to improve the optimization efficiency, in which the two-point adding point criterion has been utilized. To maximize the lift of the leading car and minimize the drag of the whole train, the optimization on a two-unit urban maglev train has been performed numerically by varying the nose height and the length of the streamline. The optimal streamlined shape has been obtained within the limited design space which meets the engineering constraint requirement. Several conclusions are drawn as follows.

(1) Through the validations of wind tunnel experiments and test functions with analytical solutions, the numerical methods and the optimization strategy have been successfully proven to be highly efficient and accurate and be applicable to practical engineering problems.
(2) The LSF method can be used with easy access to obtain new shapes with smooth and reasonable surfaces. The variation of design variables can ensure the continuity of three-dimensional surfaces. LSF method is suitable for aerodynamic shape optimization of urban maglev trains.
(3) The aerodynamic performance of the optimal shape has been improved significantly. Compared to the prototype, the aerodynamic lift of the leading car has been increased by 33.25%, the aerodynamic lift of the trailing car has been reduced by 1.78%, and the drag of the whole train has been reduced by 4.44%.
(4) The length of the streamline shows little influence on aerodynamic lift of the leading car but great influence on the drag of the whole train. The nose height affects severely both aerodynamic lift of the leading car and drag of the whole train, and strong nonlinear relationship is observed, which should be specifically studied during the optimal design of urban maglev trains.

In general, aerodynamic performance of the urban maglev train can be substantially improved by optimizing the streamlined shape. The optimization strategy proposed in the present paper can be utilized for the shape design of urban maglev trains and further extended to engineering applications.

Acknowledgements This work was supported by Advanced Rail Transportation Special Plan in National Key Research and Development Project (Grants 2016YFB1200601-B13 and 2016YFB1200602-09) and Youth Innovation Promotion Association CAS (2019020). And Computing Facility for the "Era" petascale supercomputer of Computer Network Information Center of Chinese Academy of Sciences is gratefully acknowledged.

References

1. Spiryagin, M., Persson, I., Hayman, M., et al.: Friction measurement and creep force modelling methodology for locomotive track damage studies. Wear **432**–**433**, 202932 (2019)
2. Fang, X.C., Lin, S., Yang, Z.P., et al.: Adhesion control strategy based on the wheel-rail adhesion state observation for high-speed trains. Electronics **7**(5), 70 (2018)
3. MBB aktuell. Das MBB Prinzipfahrzeug [N]. Firmenzeitung Messerschmitt-Bölkow-Blohm GmbH (1971).
4. HSST magnetic levitation trains: past, present and future. Society of Automotive Engineers, Inc. (1990).
5. Tyll, J.S., Liu, D., Schetz, J.A., et al.: Experimental studies of magnetic levitation train aerodynamics. AIAA **34**(12), 2465–2470 (1996)
6. Huang, S., Li, Z.W., Yang, M.Z.: Aerodynamics of high-speed maglev trains passing each other in open air. J. Wind Eng. Ind. Aerodyn. **188**, 151–160 (2019)
7. Gao, D.G., Ni, F., Lin, G.B., et al.: Aerodynamic analysis of pressure wave of high-speed maglev vehicle crossing: modeling and calculation. Energies **12**(19), 3770 (2019)
8. J.M. Wells, P. B. Colin. An aerodynamic study of an urban maglev vehicle. AIAA 2010-1419 (2010).
9. P.B. Colin, M.W. John, R. Benoit, et al.: Aerodynamics of urban maglev vehicles. Proceedings of the Institution of Mechanical Engineers, Part F: Journal of Rail and Rapid Transit **226**(6), 561–567 (2012).
10. Shu, X.W., Gu, C.G., Liang, X.F., et al.: Numerical simulation of aerodynamic performance of high speed maglev train with streamlined head. J. Shanghai Jiaotong Univ. (Chin. Ed.) **06**, 1034–1037 (2006). (In Chinese)
11. Yao, S.G., Xu, P.: Aerodynamic performance Analysis of domestic Maglev train. Railw. Rolling Stock **03**, 33–34 (2007). (In Chinese)
12. Zhou, D., Tian, H.Q., Lu, Z.J.: Optimization of aerodynamic shape of domestic maglev train. J. Central S. Univ. (Natural Science Edition) **03**, 613–617 (2006)
13. Kwon, H.B., Jang, K.H., Kim, Y.S., et al.: Nose shape optimization of high-speed train for minimization of tunnel sonic boom. Jpn. Soc. Mech. Eng. **4**, 890–899 (2001)
14. Lee, J.: Approximate optimization of high-speed train nose shape for reducing micropressure wave. Ind. Appl. **35**, 79–87 (2008)

15. Kim, I., Ok, H.: A study on the aerodynamic characteristics of a high speed train entering a tunnel and frontal shape optimization. J. KSAS **26**(1), 17–26 (1998)
16. V.V. Vytla, P.G. Huang, R.C. Penmetsa: Multi objective aerodynamic shape optimization of high speed train nose using adaptive surrogate model, in: 28th AIAA Applied Aerodynamics Conference, 28 June-01 July, Chicago, Illinois (2010)
17. Krajnović, S.: Shape optimization of high-speed trains for improved aerodynamic performance. P I Mech. Eng. F – J. Rai. **223**, 439–452 (2009)
18. Ku, Y.C., Kwak, M.H., Park, H.I. et al.: Multi-objective optimization of highspeed train nose shape using the vehicle modeling function. In: 48th AIAA aerospace sciences meeting, Orlando (2010)
19. Li, R., Xu, P., Peng, Y., et al.: Multi-objective optimization of a high-speed train head based on the FFD method. J. Wind Eng. Ind. Aerodyn. **152**, 41–49 (2016)
20. Zhang, Y., Yang, G.W., Guo, D.L., et al.: A novel CACOR-SVR multi-objective optimization approach and its application in aerodynamic shape optimization of high-speed train. Soft Comput. **23**, 1–17 (2019)
21. Paniagua, J.M., García, J.: Aerodynamic surrogate-based optimization of the nose shape of a high-speed train for crosswind and passing-by scenarios. J. Wind Eng. Ind. Aerodyn. **184**, 139–152 (2019)
22. Muñoz-Paniagua, J., García, J.: Aerodynamic drag optimization of a high-speed train. J. Wind Eng. Ind. Aerodyn. **204**, 104215 (2020)
23. Yao, S.B., Guo, D.L., Sun, Z.X., et al.: Parametric design and optimization of high speed train nose. Optim. Eng. **17**(3), 605–630 (2016)
24. Zhang, L., Zhang, J.Y., Li, T., et al.: A multi-objective aerodynamic optimization design of a high-speed train head under crosswinds. J. Rail Rapid Transit **232**(3), 895–912 (2018)
25. Yu, M.G., Zhang, J.Y., Zhang, W.H.: Multi-objective optimization design method of the high-speed train head. J. Zhejiang Univ.-SCIENCEA (Applied Physics & Engineering) **14**(9), 631–641 (2013)
26. Luo, X., Ye, W., Huang, R., et al.: Numerical investigations of the energy performance and pressure fluctuations for a waterjet pump in a non-uniform inflow. Renew. Energy **153**, 1042–1052 (2020)
27. Li, T., Qin, D., Zhang, J.Y.: Effect of RANS turbulence model on aerodynamic behavior of trains in crosswind. Chin. J. Mech. Eng. **32**, 85–96 (2019)
28. Menter, F.R.: Two-equation eddy-viscosity turbulence models for engineering applications. AIAA **32**(8), 1598–1605 (1994)
29. Liu, H., Biglari, M., Elkamel, A., et al.: The impacts of standard wall function and drag model on the turbulent modelling of gas–particle flow in a circulating fluidised bed riser. Can. J. Chem. Eng. **91**, 704–717 (2013). https://doi.org/10.1002/cjce.21782
30. Xu, G., Liang, X.F., Yao, S.B., et al.: Multi-objective aerodynamic optimization of the streamlined shape of high-speed trains based on the Kriging model. PloS one **12**(1), e0170203 (2017)
31. Hastie, T., Tibshrani, R., Friedman, J.: The Elements of Statistical Learning: Data Mining, Inference, and Prediction. Springer, New York (2001)
32. Seymour, G.: A predictive approach to the random effect model. Narnia **61**(1), 101–107 (1974)
33. Shao, J.: Linear model selection by cross-validation. J. Am. Stat. Assoc. **88**(422), 486–494 (1993)
34. Kohavi, R.: A study of cross-validation and bootstrap for accuracy estimation and model selection. International Joint Conference on Artificial Intelligence (1995).
35. Li, J.H., Wang, R.B., Wang, W.L., et al.: Study on automatic tagging of semantic roles in Chinese frames. J. Softw. **30**(4), 597–611 (2010). (In Chinese)
36. Gao, Y.H., Wang, X.C.: Multi-point plus point sequence optimization method based on Kriging proxy model. Eng. Mech. **29**(04), 90–95 (2012). (In Chinese)
37. Holland, J.H.: Adaptation in Natural and Artificial Systems: An Introductory Analysis with Applications to Biology, Control, and Artificial Intelligence MIT Press (1975).
38. Deb, K., Pratap, A., Agarwal, S., et al.: A fast and elitist multiobjective genetic algorithm: NSGA-II. IEEE Trans. Evol. Comput. **06**, 182–197 (2002)